Journal of Atmospheric and Solar-Terrestrial Physics 77 (2012) 125–131

Contents lists available at SciVerse ScienceDirect

Journal of Atmospheric and Solar-Terrestrial Physics

journal homepage: www.elsevier.com/locate/jastp

# Improvement to the global distribution of coronal plasma and magnetic field on the source surface using expansion factor $f_s$ and angular distance $\theta_b$

Fang Shen*, Xueshang Feng, Changqing Xiang

*State Key Laboratory of Space Weather, Center for Space Science and Applied Research, Chinese Academy of Sciences, Beijing 100190, China*

ARTICLE INFO

*Article history:*
Received 30 August 2011
Received in revised form
29 November 2011
Accepted 13 December 2011
Available online 27 December 2011

*Keywords:*
Global coronal plasma and field distribution
Expansion factor $f_s$
Angular distance $\theta_b$

ABSTRACT

In this paper, we have developed an improved model to build a self-consistent global structure on the source surface of 2.5 Rs covering four different phases of solar activity. This model involves the topological effect of the magnetic field expansion factor $f_s$ and the minimum angular distance $\theta_b$ (at the photosphere) between an open field foot point and its nearest coronal hole boundary. The purpose of this effect is to separate the open field area and the close field area more effectively. The model uses as input for 136 Carrington Rotations (CRs) covering four different phases of solar activity: (1) an empirical model of the magnetic field topology on the source surface using Line-of-sight (los) photospheric field ($B_{los}$) measurements by Wilcox Solar Observatory (WSO); and (2) an empirically derived global coronal density distribution using K coronal polarized brightness ($pB$) by MKIII in High Altitude Observator (HAO). The solar wind speed on the source surface is specified by the function of both $f_s$ and $\theta_b$, which are obtained by the magnetic field data. Then the coronal mass outputs are analyzed and the self-consistent global distribution on the source surface is numerically studied for the four different phases. Finally, the model estimates the solar wind speed at 1 AU as a simple function of the speed on the source surface. Our numerical results indicate reasonable semi-quantitative agreement with observations at different phases of solar activity.



## 1. Introduction

The study for the self-consistent global distribution of the magnetic structures and the fluid fields (such as the density, the temperature, the velocity field and the coronal mass outputs) on the source surface is an important topic in determining the initial boundary conditions of constructing three-dimensional (3D) structures near the Sun and in the heliosphere (Priest et al., 1998); and even in improving space weather prediction level (Dryer, 1994; Guo and Wu, 1998; Wei et al., 2003). At present, although in-situ observations near the Sun are not available due to the limitations of space measurements, much progress in this topic has still been made (Odstrcil et al., 2004; Owens et al., 2008; Hu et al., 2008; Shen et al., 2010).

Recently, we studied the basic characteristics of the global distribution for the corona plasma and magnetic field near 2.5 Rs with the statistical and numerical methods (Shen et al., 2010, hereinafter referred to as paper 1). In paper 1, although the current sheet region and the coronal hole region were separated by the density value, the solar wind speed at 1 AU deduced from the speed on the source surface of 2.5 Rs existed much discrepancy compared with the observation. Here, much improvement is made to remedy the discrepancy. In order to empirically specify the open field region and the close field region by considering the magnetic field topology effects, we follow the work of Feng et al. (2010, 2011) on the expansion factor $f_S$ and the angular distance $\theta_b$.

There exists a close relationship between the solar wind velocity and the inverse of the expansion factor $f_S$ (Levine et al. 1977; Wang and Sheeley, 1990; Arge and Pizzo, 2000) and the angular distance $\theta_b$ (Arge et al., 2003; Feng et al., 2010). The expansion factor $f_S$ (Wang and Sheeley, 1990) can be written as $f_S=(R_S/r)^2(B_{R_S}/B_r)$, where $R_S$ and $r$ are the solar radius and the distance from the solar center; $B_{R_S}$ and $B_r$ are magnetic field strengths at the source surface (2.5 Rs) and at $r$. The angular distance $\theta_b$ denotes the minimum angular separation (at the photosphere) between an open field foot point and its nearest coronal hole boundary. It can be used to distinguish the high-speed solar winds from the low-speed solar wind (high-speed stream originating from the center of an open field region has large $\theta_b$ and low-speed stream from the hole boundary has a small $\theta_b$).

The purpose of the present paper is to find an improved method to analyze the global distribution of coronal plasma and magnetic field on the source surface spanning all phases of solar activities. In order to separate the open field region and the close

* Corresponding author. Tel.+ 8610 6258 6353.
*E-mail addresses:* fshen@spaceweather.ac.cn (F. Shen), fengx@spaceweather.ac.cn (X. Feng), cqxiang@spaceweather.ac.cn (C. Xiang).

1364-6826/$ - see front matter © 2011 Elsevier Ltd. All rights reserved.
doi:10.1016/j.jastp.2011.12.009

field region effectively, we use the expansion factor $f_S$ and the angular distance $\theta_b$ in specifying the solar wind speed on the source surface. The solar wind speed at 1 AU derived from the new distribution on the source surface works much better than the one derived from the previous method, as compared with the observational data.

## 2. Approach

This present study selects the same time interval of 136 CRs (CRs 1811 to 1946) as that in paper 1, which spans the middle latter portion of solar cycle 22 (January, 1989–April, 1995) and the former portion of solar cycle 23 (May, 1995–March, 1999). The selected CRs can be broadly grouped into four categories according to the solar activities (paper 1): the solar maximum (CRs 1811–1825), the descending phase (CRs 1826–1904), the solar minimum (CRs 1905–1925) and the ascending phase (CRs 1926–1946).

Based on the observational data, the statistical average results of magnetic field and density distribution on the source surface are achieved separately during the four different phases, just like paper 1. The distributions of the radial magnetic field $B_r$ at 2.5 Rs for every CR can be determined using the line-of-sight (los) photospheric field ($B_{\rm los}$) measurements, which was made at Wilcox Solar Observatory (WSO), and the potential field source surface (PFSS) model (Luhmann et al. 2002; Zhao et al. 2006; Hu et al. 2008). The global density distribution at 2.5 Rs can be adopted from the observational data of K coronal polarized brightness ($pB$) by MKIII in High Altitude Observator (HAO). Following the solar wind density model constructed by Guhathakurta et al. (1996), the coronal density from 1 Rs to 5.5 Rs is roughly given (Xiang et al., 2006):

$$N(r,\theta,\varphi)=\begin{cases} N_{cs}\left[\frac{I_{pB}(r_0,\theta,\varphi)}{I_{pB_{cs}}}\right]^{1/2} & \text{(coronalstreamer belt)}\\ N_h\left[\frac{I_{pB}(r_0,\theta,\varphi)}{I_{pB_h}}\right]^{1/2} & \text{(coronal hole region)}\\ N_h+(N_{cs}-N_h)e^{-4[(I_{pB}(r_0,\theta,\varphi)-I_{pB_{cs}})/(I_{pB_{cs}}+I_{pB_h})]^2} & \text{(other region)}\end{cases} \quad (1)$$

where $(r,\theta,\varphi)$ denoted the spherical coordinate system with its origin at the Sun's center. $r_0=1.36$ Rs, $I_{pB}$ denotes the observation value of $pB$ at 1.36 Rs and $N_{cs}$, $N_h$ are the electron densities at the current sheet and the polar holes, which were expressed in detail by Guhathakurta et al. (1996). The top panels (a–d) and bottom panels (e–h) of Fig. 1 (Figure 2 in paper 1) can illustrate how the magnetic structure and the density distribution on the source surface of 2.5 Rs evolve during the four phases of the solar cycle, respectively.

Then, we adopt the solar wind speed at 2.5 Rs by means of the magnetic field expansion factor $f_s$ and the angular distance $\theta_b$. Here we also use PFSS model (Luhmann et al. 2002; Zhao et al. 2006; Hu et al. 2008) to determine $f_s$ and $\theta_b$ at 2.5 Rs, because the output of the PFSS model can provide a more realistic magnetic field topology of the upper corona. And beyond 2.5 Rs, $f_S$ and $\theta_b$ take their distributions on the source surface (Feng et al., 2010, 2011). The following empirical relationship (Owens et al., 2005; also used by Feng et al., 2010) is used to assign solar wind speed at a radius of 5 Rs in this study:

$$V(f_S,\theta_b)=265+\frac{1.5}{(1+f_S)^{2/7}}\{5.8-1.6e^{[1-(\theta_b/7.5)^3]}\}^{3.5} \quad \text{(km/s)} \quad (2)$$

with the help the expansion factor $f_s$ and the angular distance $\theta_b$ (with the unit of degree). It should be pointed out that our data origin of Eq. (2) is from WSO data, which is different with that of Owens et al., (2005). From top to bottom, Fig. 2 displays the distribution of the number density, the magnetic field, the expansion factor $f_s$, the angular distance $\theta_b$ at 2.5 Rs and the solar wind speed at 5 Rs, during CR 1823 (at the solar maximum, (a)), CR 1874 (at the descending phase, (b)), CR 1910 (at the solar minimum, (c)) and CR 1932 (at the ascending phase, (d)), respectively.

Using the mass conservation relation, $nvr^2\big|_{r=2.5R_S}=nvr^2\big|_{r=5R_S}$, we can derive the solar wind speed on the source surface at 2.5 Rs from the physical conditions at 5 Rs, where the density $n$ at 5 Rs is calculated from Eq. (1). Fig. 3(a)–(d) gives the average radial solar wind speed distribution on the source surface over the four phases of solar activity. Through comparing Fig. 3 with the top panels of Fig. 1, we find that as the expansion factor $f_s$ and the angular distance $\theta_b$ are used to assign solar wind speed, the low speed regions are basically associated with the coronal current sheet area, and the high speed regions are always associated with the coronal hole area, no matter at the minimum, descending phase, ascending phase or the maximum.

Then, we can obtain the average solar plasma mass flux,

$$F_{m_i}(2.5\ \text{Rs},\theta,\varphi)=(n(2.5\ \text{Rs},\theta,\varphi)v(2.5\ \text{Rs},\theta,\varphi))_i (i=1,2,3,4),$$

on the source surface over the four phases, according to the observations of the K coronal brightness and the solar plasma speed, where $(n(2.5\ \text{Rs},\theta,\varphi)\ v(2.5\ \text{Rs},\theta,\varphi))_i$ denote the average solar plasma mass flux at 2.5 Rs over the maximum ($i=1$), the descending phase ($i=2$), the minimum ($i=3$) and the ascending phase ($i=4$) of solar activity, separately.

Based on the statistical average results of the magnetic field, the density and the coronal mass outputs flux pattern at 2.5 Rs for the four different phases of solar activities, by referring to e.g., Wei et al. (2003) and paper 1, our self-consistent model for coronal physical parameters on the source surface can be written

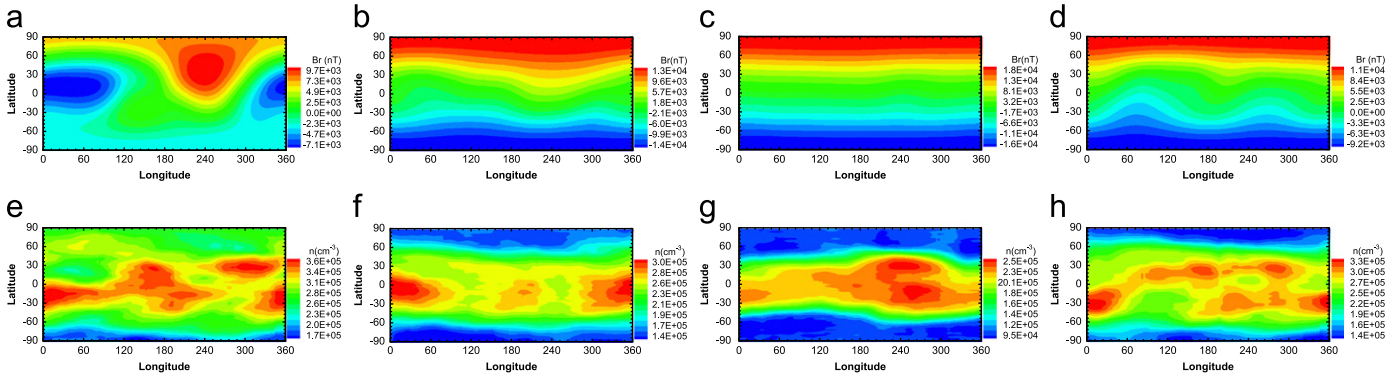


**Fig. 1.** Average distributions of the radial magnetic fields $B_r$ and density over the four different phases: Maximum, descending phase, minimum and ascending phase of solar activities.

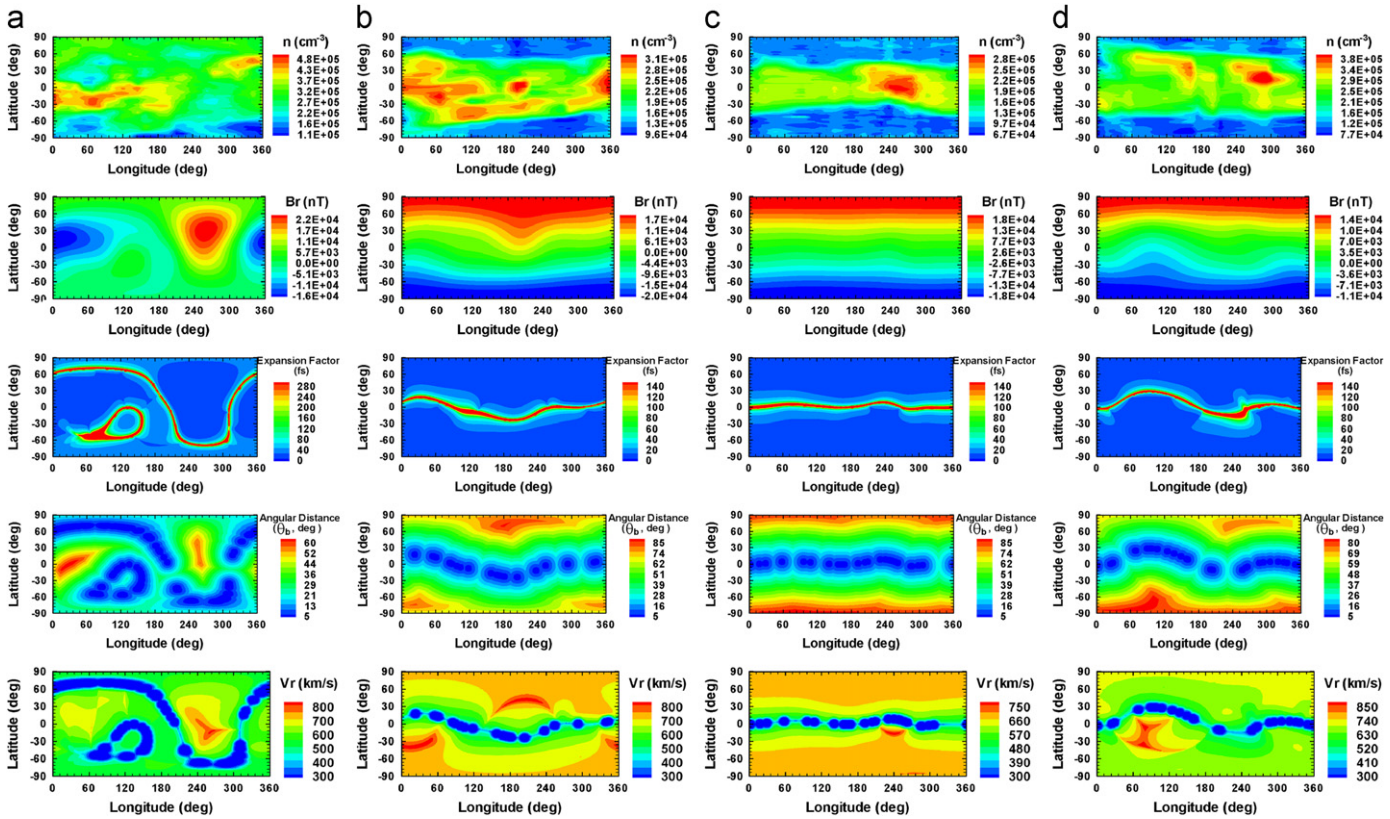


**Fig. 2.** Distribution of the number density, the magnetic field, the expansion factor $f_s$, the angular distance $\theta_b$ at 2.5 Rs and the solar wind speed at 5 Rs, during (a) CR 1823 (maximum), (b) CR 1874 (descending phase), (c) CR 1910 (minimum) and (d) CR 1932 (ascending phase), respectively.

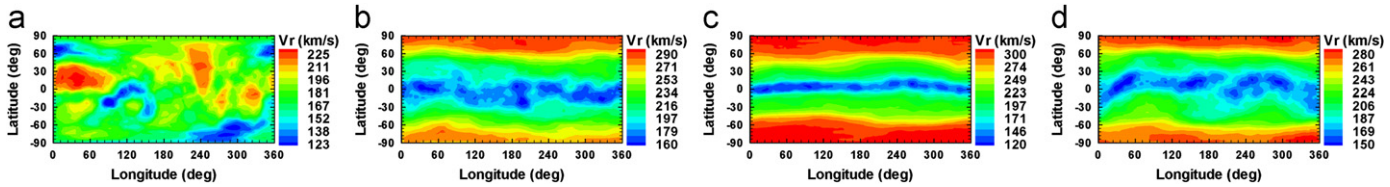


**Fig. 3.** Average distributions of the radial solar speed over the four different phases: (a) maximum, (b) descending phase, (c) minimum and (d) ascending phase of solar activities.

in 1D ideal MHD equations:

$$v\frac{\partial n}{\partial r}+n\frac{\partial v}{\partial r}+2nv/r=0, \tag{3}$$

$$nv\frac{\partial v}{\partial r}+\frac{\partial p}{\partial r}+ng=0, \tag{4}$$

$$n\frac{\partial p}{\partial r}-\gamma p\frac{\partial n}{\partial r}=0, \tag{5}$$

$$r\frac{\partial B}{\partial r}+2B=0, \tag{6}$$

$$p=2\Re' nT, \tag{7}$$

$$\frac{\partial p}{\partial r}=2\Re' T\frac{\partial n}{\partial r}+2\Re' n\frac{\partial T}{\partial r}, \tag{8}$$

$$\beta(B)=8\pi p/B^2, \tag{9}$$

$$nv=F_{m_c}(F_{m_i},f_s,\theta_b) \tag{10}$$

here Eqs. (3)–(9) were used in paper 1, in which Eq. (9) was the statistical results for the plasma beta $\beta$ and $\gamma$ =1.4 (paper 1).

From the previous studies by Arge et al. (2003) and Owens et al., (2005), there exist the inverse correlation between the expansion factor $f_s$ and speed, and positive correlation between the angular distance $\theta_b$ and speed. Here, for the distribution for the coronal mass output flux $F_{m_c}$ in Eq. (10), We chose the function:

$$F_{m_c}(F_{m_i},f_s,\theta_b)=F_{m_i}\frac{{\theta_b}^{0.2}}{(1+f_s)^{1/3}} \tag{11}$$

to deduce the speed at 2.5 Rs $v_r=F_{m_c}/n$, whose purpose is to get the obvious correspondence between the coronal current sheet and the small velocity region; and between the polar coronal hole and the large velocity region, during all the solar cycle. In Eq. (11), $i$=1, 2, 3 and 4 denote the average solar plasma mass flux over the maximum, the descending phase, the minimum and the ascending phase of solar activity, separately. It is a function of three coronal parameters, the average coronal mass outputs flux ($F_{m_i}$), the expansion factor ($f_s$) and the angular distance ($\theta_b$, measured in degrees). This relationship quite differs from that in paper 1.

The other 10 unknown parameters, $B$, $\partial B/\partial r$, $v$, $\partial v/\partial r$, $T$, $\partial T/\partial r$, $n$, $\partial n/\partial r$, $p$ and $\partial p/\partial r$, can be found if any two of them are known by solving governing Eqs. (3)–(10). In the case investigated, the magnetic field $B$ and density $n$ are two known inputs on the source surface at

2.5 Rs, which are calculated in the previous section. In the following computation, the source surface is divided into $182 \times 92$ cells with each being $2^\circ \times 2^\circ$.

## 3. Results

Based on the statistical average distributions of the radial magnetic field $B_r$, the numerical density $n$ and the coronal mass flux $F_{m_c}$ on the source surface at 2.5 Rs, and the self-consistent MHD equations mentioned above, the numerical results of other parameters, such as the temperature and the radial velocity on the source surface can be deduced during every CR at the solar maximum, the descending phase, the solar minimum, and the ascending phase.

From top to bottom, Fig. 4 gives the numerical results of global distribution for the temperature $T$, the radial velocity $v_r$ and the

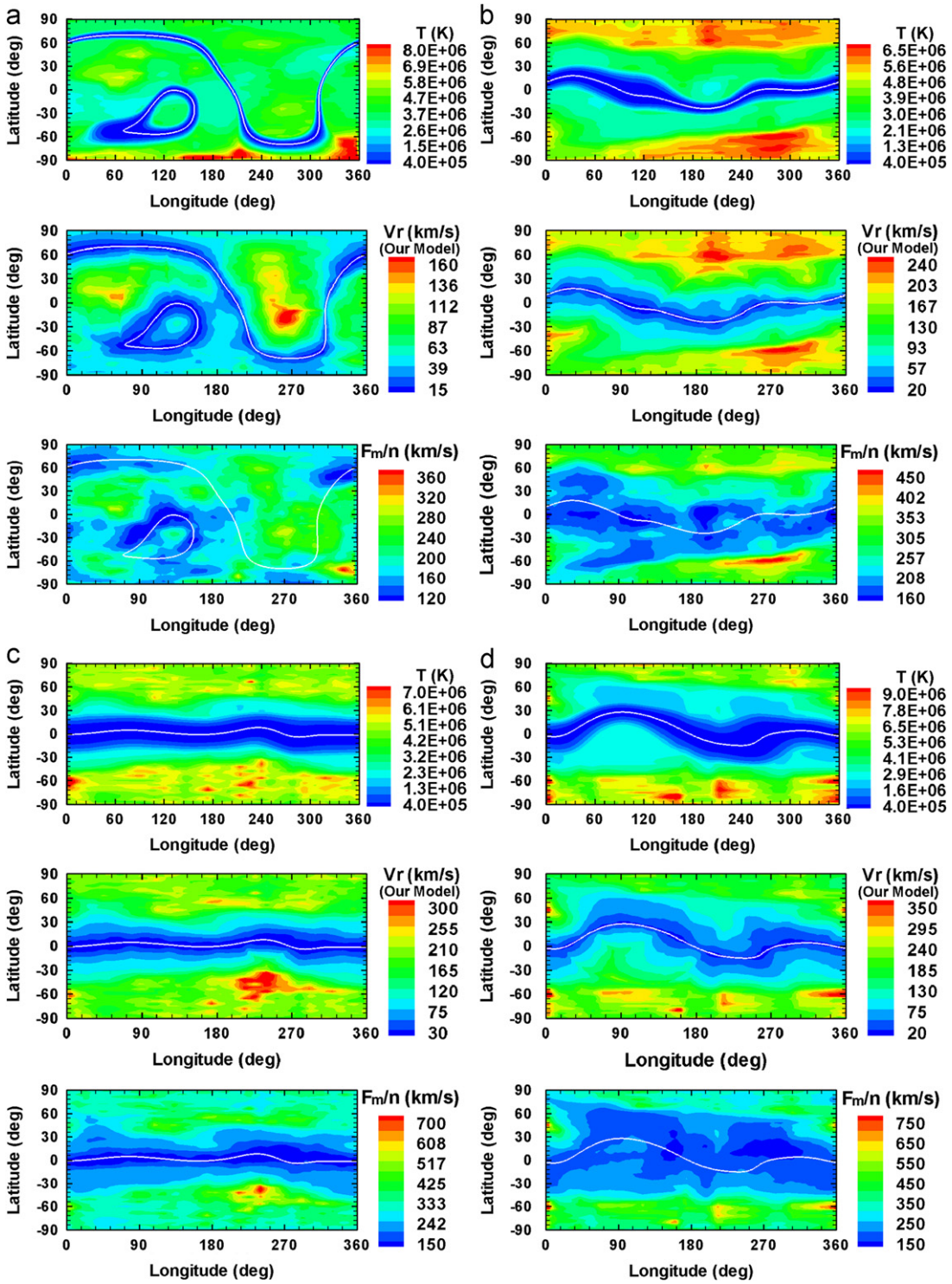


**Fig. 4.** Distribution of (from top to bottom) the temperature, the radial velocity $v_r$, and the value $F_{m_i}/n$ on source surface of 2.5 Rs from numerical simulation at (a) CR 1823 in 1989 (maximum); (b) CR 1874 in 1993 (descending phase); (c) CR 1910 in 1996 (minimum); and (d) CR 1932 in 1998 (ascending phase). The white lines in each panel denote the coronal current sheets.

value $F_{m_i}/n$ on the source surface of 2.5 Rs during CR 1823 (at the solar maximum, $i=1$, (a)), CR 1874 (at the descending phase, $i=2$, (b)), CR 1910 (at the solar minimum, $i=3$, (c)) and CR 1932 (at the ascending phase, $i=4$, (d)), respectively. For comparison, the coronal current sheets in the panels are shown with the white lines. From the top two rows in Fig. 4, we find the minimum temperature and velocity region are related to the coronal current sheet region at the solar minimum, the descending phase, the ascending phase and the solar maximum. We also recognize that at all phases, the flow speed and temperature are lower in the neighborhood of the coronal current sheet and higher at the polar regions, which is qualitatively in agreement with the observed intensity pattern (Kojima et al., 1998, 2001). The high temperature and velocity regions, with most of the low density regions, are basically located at the polar coronal hole regions, from the results of the number density shown in the top panels of Fig. 2, the temperature and radial speed shown in the top two rows of Fig. 4 together with the location of the coronal current sheets. The regions where the temperature and velocity are too high are limited to the very small area of the polar coronal hole. In addition, we can observe that where the solar activity level increases, the high speed stream area reduces while the high density area changes reversely.

From comparing the middle and the bottom rows of Fig. 4, there exist obvious differences between $F_{m_i}/n$ (speed without correction) and $v_r(=F_{m_i}/n)$. With correction to the average coronal mass outputs flux $F_{m_i}$, the velocity deduced by $F_{m_i}/n$ can show the obvious correspondence between the coronal current sheet and the small velocity region; and between the polar coronal hole and the large velocity region, during all the solar cycle. We can find that the lower-speed region (corresponding to coronal current sheet region) in the bottom panels are quite thinner than that in the middle panels.

The solar wind speed at 1 AU is obtained by mapping the speed on the source surface of 2.5 Rs to that at the earth orbit through a linear relation:

$v(1\ \mathrm{AU})=c_1\times\ v(2.5\ \mathrm{Rs})+255$, where

(1) $c_1=3.15$ at the solar maximum;
(2) $c_1=4.65$ at the descending and ascending phases;
(3) $c_1=9.15$, at the solar minimum.

The coefficients $c_1$ and $c_2$ are estimated by means of the radial speed relation of the solar wind (Withbroe, 1988). This relation is also similar in form to that in paper 1 and Wei et al. (2003). We were also interested in comparing our improved numerical speed at 1 AU with observational data, WSA model and that in paper 1.

Paper 1 compared the predicted solar wind speed with WSA model and observations for the years 1989–1990, 1993, 1995–1998, which goes through the solar maximum, the descending phase, the solar minimum and the ascending phase. Following paper 1, Fig. 5 (long period) and Fig. 6 (short period) compare the solar wind speed at 1 AU observed by IMP 8 (1989–1990) and WIND (1995, 1997–1998) (red) with solar wind speed predictions from the present model (black) and paper 1 (blue) and using the WSA velocity relationship (Arge et al., 2003) (only in Fig. 6, green),

$$V(f_S,\theta_b)=265+\frac{25}{f_S^{2/7}}\{5-1.1e^{[1-(\theta_b/4)^2]}\}^2\ \mathrm{km/s},$$

where $f_s$ is the magnetic expansion factor (Wang and Sheeley, 1990; Arge and Pizzo, 2000) and $\theta_b$ is the angular distance (Arge et al., 2003). Here, both $f_s$ and $\theta_b$ are calculated based on the WSO data, which were analyzed in detail in Part 2.

Solar wind speed predictions obtained by the improved numerical model show better agreement with observations and the WSA model than those obtained in paper 1 (see Figs. 5 and 6). The improved model provides a clear improvement over paper 1 in all solar phases, including the solar maximum (a), the descending phase (b), the solar minimum (c) and the ascending phase (d).

Most of the highest observed solar wind speeds are due to the passage of Interplanetary Coronal Mass Ejections (ICMEs) excluded from improved numerical model. Despite the presence of ICMEs, the black curves can reproduce many of the recurring highspeed streams. In this context, the self-consistent, global distributions on the source surface of 2.5 Rs during all the phases of solar cycle could be used for understanding the change of the interplanetary condition.

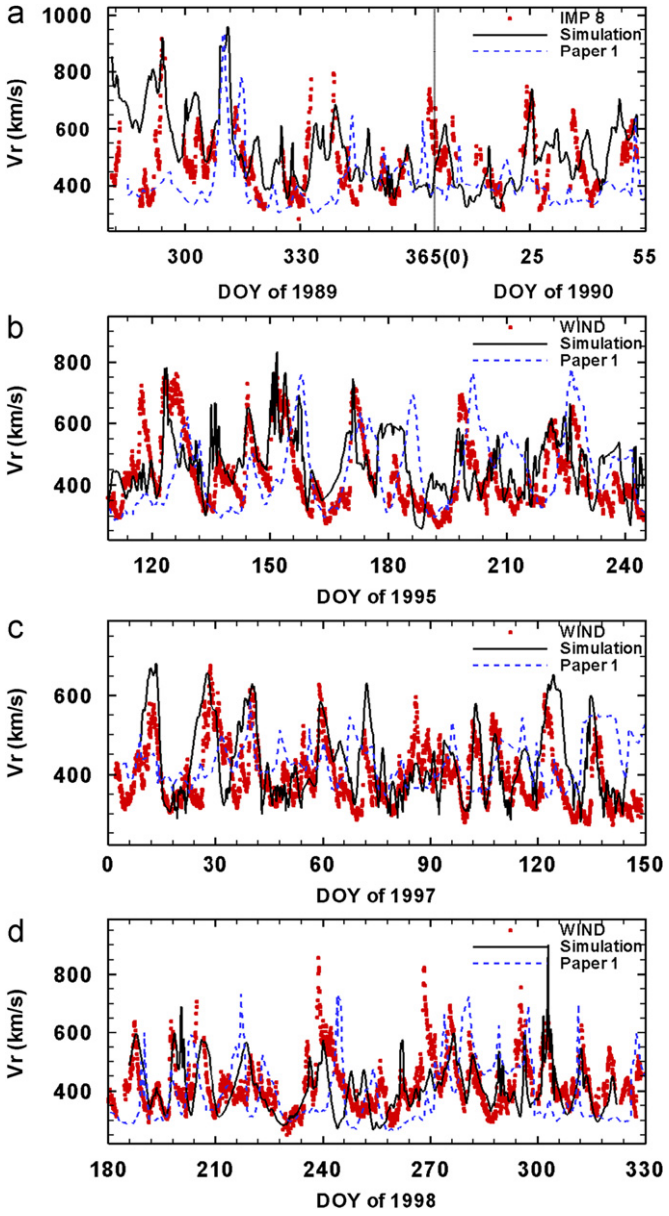


**Fig. 5.** Comparison of solar wind speed predictions from our model (black lines) and paper 1 (blue dashed lines), and the observational speed (red dots) at 1 AU during four long-time intervals: (a) DOY 281–365 of 1989 and DOY 0–55 of 1990 (maximum); (b) DOY 109–245 of 1995 (descending phase); (c) DOY 0–150 of 1997 (minimum); and (d) DOY 180–330 of 1998 (ascending phase) (For interpretation of the references to color in this figure legend, the reader is referred to the web version of this article.).

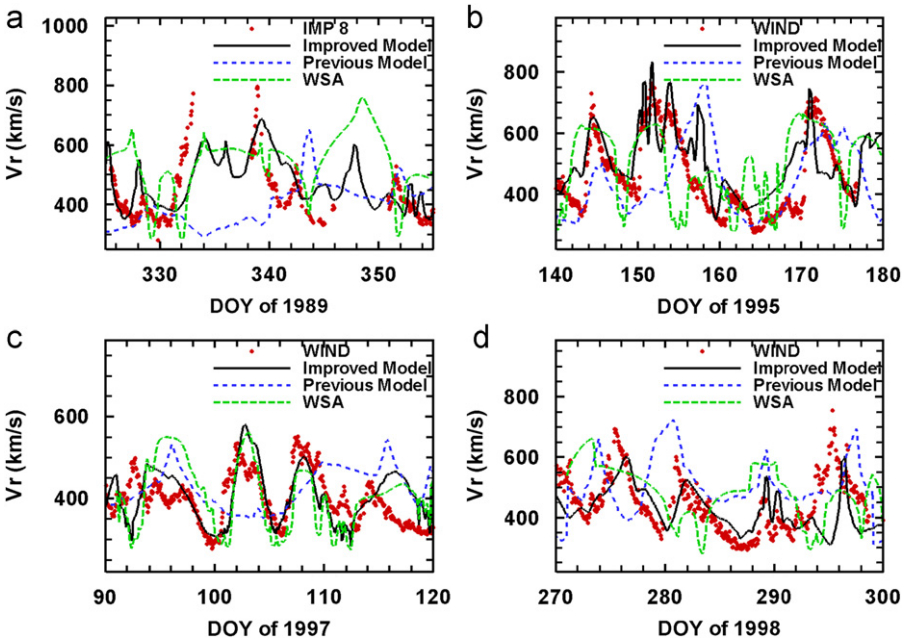


**Fig. 6.** Comparison of solar wind speed predictions from our model (black lines) and paper 1 (blue dashed lines), the observational speed (red dots) and the simulated speed by WSA model (green long-dashed lines) at 1 AU during four short-time intervals: (a) DOY 325–355 of 1989; (b) DOY 140–180 of 1995; (c) DOY 90–120 of 1997; and (d) DOY 270–300 of 1998. (For interpretation of the references to color in this figure legend, the reader is referred to the web version of this article.)

However, like other models, this improved model results still have quantitative differences from the observations. In particular, the fast solar wind speed in the model at the solar maximum is low compared to measurements. They are maybe caused by the neglect of some physical detail near the Sun; the dynamic process between 2.5 Rs and interplanetary space near 1 AU, such as the ICME. Our next goal is to couple this more realistic, solar-activity-dependent, self-consistent source surface model with the 3D MHD code to study the solar wind ambient, that is, to employ the source surface model's results as input to drive the 3D MHD model. The preliminary works have convinced us that using such inner-boundary condition could helpfully improve the capability of 3D MHD model for the corona and heliosphere.

## 4. Conclusions

In this paper, we have developed an improved model to build a self-consistent global structure on the source surface of 2.5 Rs covering four different phases of solar activity by involving the topological effect of $f_s$ and $\theta_b$. We analyze the coronal mass outputs and numerically study the self-consistent global distribution on the source surface for 136 CRs covering four different phases of solar activity. Finally, we also estimate the solar wind speed at 1 AU as a simple function of the speed on the source surface. By comparing the results from this model with observational data, we find that the solar wind speed deduced from this improved model works much better than that from paper 1. The magnetic field expansion factor $f_s$ and the angular distance $\theta_b$ can be used to separate the open–close field area on the source surface more effectively. Further we will use this improved self-consistent source surface model during all phases of solar cycle as an inner-boundary condition for 3D MHD simulation, and use it to improve the capability of 3D MHD model for predicting the interplanetary condition.

## Acknowledgments

It should be acknowledged that the contours of K corona white light brightness at 1.36 Rs are obtained from the Mauna Loa Solar Observatory (HAO/NCAR), solar photospheric magnetic field data are from Wilcox Solar Observatory (WSO), and solar wind speeds at 1 AU are taken from the observation data of Wind spacecraft and IMP 8 satellite. This work is jointly supported by National Natural Science Foundation of China (40921063, 41074121, 41174150, 41031066, 40874077, 40890162 and 40874091), the 973 project under grant 2012CB825601, and the Specialized Research Fund for State Key Laboratories and the Public Science and Technology Research Funds Projects of Ocean (201005017).

## References

Arge, C.N., Pizzo, V.J., 2000. Improvement in the prediction of solar wind conditions using near-real time solar magnetic field update. Journal of Geophysical Research 105 (A5), 10465–10479.

Arge, C.N., D. Odstrcil, V.J. Pizzo, and L.R. Mayer (2003), Improved method for specifying solar wind speed near the Sun. In: M. Velli, R. Bruno, and F. Malara (Eds.), Solar Wind Ten, AIP Conference Proceedings, vol. 679, pp. 190–193.

Dryer, M., 1994. Interplanetary studies: Propagation of disturbances between the Sun and the magnetosphere. Space Science Review 67, 363–419.

Feng, X., et al., 2010. Three-dimensional solar wind modeling from the sun to earth by a SIP-CESE MHD model with a six-component grid. Astrophysics Journal 723, 300–319. doi:10.1088/0004-637X/723/1/300.

Feng, X., Zhang, S., Xiang, C., Yang, L., Jiang, C., Wu, S.T., 2011. A hybrid solar wind model of the cese+hll method with a Yin–Yang overset grid and an AMR grid. Astrophysics Journal 734 (1), 50. doi:10.1088/0004-637X/734/1/50.

Guhathakurta, M., Holzer, T.E., MacQueen, R.M., 1996. The large-scale density structure of the solar corona and the heliospheric current sheet. Astrophysics Journal 459, 817–831.

Guo, W.P., Wu, S.T., 1998. A magnetohydrodynamic description of coronal helmet streamers containing a cavity. The Astrophysical Journal 494, 419–429.

Kojima, M., Tokumaru, M., Watanabe, H., Yokobe, A., Asai, K., Jackson, B.V., Hick, P.L., 1998. Heliospheric tomography using interplanetary scintillation observations: 2. Latitude and heliocentric distance dependence of solar wind structure at 0.1–1 AU. Journal of Geophysical Research 103 (A2), 1981–1989.

Kojima, M., Fujiki, K., Ohmi, T., Tokumaru, M., Yokobe, A., Hakamada, K., 2001. Latitudinal velocity structures up to the solar poles estimated from interplanetary scintillation tomography analysis. Journal of Geophysical Research 106 (A8), 15677–15686.

Hu, Y., Feng, X., Wu, S.T., Song, W., 2008. Three-dimensional MHD modeling of the global corona throughout solar cycle 23. Journal of Geophysical Research 113, A03106.

Levine, R.H., Altschuler, M.D., Harvey, J.W., 1977. Solar sources of the interplanetary magnetic field and solar wind. Journal of Geophysical Research 82 (7), 1061–1065.

Luhmann, J.G., Li, Y., Arge, C.N., Gazis, P.R., Ulrich, R., 2002. Solar cycle changes in coronal holes and space weather cycles. Journal of Geophysical Research 107 (A8), 1154. doi:10.1029/2001JA007550.

Odstrcil, D., Pizzo, V.J., Linker, J.A., et al., 2004. Initial coupling of coronal and heliospheric numerical magnetohydrodynamic codes. Journal of Atmospheric and Solar Terrestrial Physics 66, 1311–1320.

Owens, M.J., Arge, C.N., Spence, H.E., Pembroke, A., 2005. An event-based approach to validating solar wind speed predictions: high-speed enhancements in the Wang–Sheeley–Arge model. Journal of Geophysical Research 110, A12105.

Owens, M.J., Spence, H.E., Mcgregor, S., et al., 2008. Metrics for solar wind prediction models: comparison of empirical, hybrid, and physics based schemes with 8 years of L1 Observations. Space Weather, 6. doi:10.1029/2007SW000380.

Priest, E.R., et al., 1998. Nature of the heating mechanism for the diffuse corona. Nature 393, 545.

Shen, F., Feng, X., Xiang, C., Song, W.B., 2010. The statistical and numerical study of the global distribution of coronal plasma and magnetic field near 2.5 Rs over a 10-year period. Journal of Atmospheric and Terrestrial Physics 72 (13), 1008–1018.

Wang, Y.M., Sheeley Jr., N.R., 1990. Solar wind speed and coronal flux tube expansion. Astrophysics Journal 355, 726–732.

Wei, F.S., Feng, X.S., Cai, H.C., Zhou, Q.J., 2003. Global distribution of coronal mass outputs and its relation to solar magnetic field structures. Journal of Geophysical Research 108 (A6), 1238. doi:10.1029/2002JA009439.

Withbroe, G.L., 1988. The temperature structure, mass and energy flow in the corona and inner solar wind. Astrophysics Journal 325, 442–467.

Xiang, C.Q., Feng, X.S., Fan, Q.L., Yao, J.S., 2006. An observation-based model of solar wind background. Chinese Journal of Space Science 26 (3), 161–166.

Zhao, X.P., Hoeksema, J.T., Liu, Y., Scherrer, P.H., 2006. Success rate of predicting the heliospheric magnetic field polarity with Michelson Doppler Imager (MDI) synoptic charts. Journal of Geophysical Research 111, A10108.